ACS APPLIED MATERIALS & INTERFACES

Research Article

www.acsami.org

Realization of ppb-Scale Toluene-Sensing Abilities with Pt-Functionalized SnO_2–ZnO Core–Shell Nanowires

Jae-Hun Kim and Sang Sub Kim*

Department of Materials Science and Engineering, Inha University, Incheon 402-751, Republic of Korea

ABSTRACT: In this paper, we report the exceptional toluene-sensing properties of SnO_2–ZnO core–shell nanowires (C–S NWs) functionalized with Pt nanoparticles (NPs). A response of 279 was obtained for 100 ppb of toluene, and to the best of our knowledge, this is the highest toluene response to be reported in the literature. The SnO_2–ZnO C–S NWs were synthesized via a two-step process: First, a networked core of SnO_2 nanowires was prepared via vapor–liquid–solid growth on the patterned electrode layer. Second, the ZnO shell layers were created with atomic layer deposition. The electron-depleted region of the shell layer was further expanded by attaching Pt NPs, which were synthesized using γ-ray radiolysis, to the shell layer. In addition to the expansion of the electron-depleted region, the catalytic effect of Pt on toluene greatly improved the toluene-sensing performance of the C–S NWs. The extraordinary toluene-sensing ability of the Pt-functionalized C–S NWs means they have great potential as the sensing platform in exhaled breath sensors to detect ppb-scale toluene.

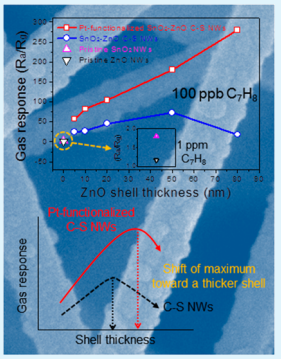

KEYWORDS: *SnO_2–ZnO, core–shell nanowire, Pt particle, gas sensor, disease diagnosis*

1. INTRODUCTION

Sensitive and reliable chemical sensors that can detect trace amounts of hazardous chemical species are required to prevent environmental pollution. A great number of materials have been tested as sensing materials over the past decades. Despite their poor selectivity, semiconducting metal oxides (SMOs) are recognized as promising materials for chemical sensors because of their excellent thermal stability, sensing reliability, low processing costs, and relatively simple operating mechanism. To maximize the sensing abilities of chemiresistive SMOs, nanomaterials, such as nanowires (NWs), nanorods, and nanofibers, have received much attention because of their unique material properties, including providing larger numbers of surface interaction sites, the faster diffusion of gas molecules, and a larger modulation of electrical resistivity compared to that of their bulk or thin-film counterparts.[1−4]

Highly networked oxide NWs have proven to be a reliable sensor platform for the detection of chemical species.[5−7] Detailed investigations into the fabrication and sensing properties of highly networked SnO_2,[8,9] CuO,[10,11] and ZnO[12,13] NWs have been performed by the current authors. In order to use chemiresistive SMO NWs in sensor devices, one of the most important issues to solve is improving their sensing performance so that extremely low concentrations of chemical species can be detected. One route for such an improvement is the application of core–shell (C–S) structures, in which the heterointerface created between the core and the shell provides an energy band structure that enhances the sensing capabilities compared to their single-structured counterparts.[14−20] As shown in the literature,[21,22] the use of C–S structures is particularly effective at enhancing the sensing performance when the thickness of the shell is similar to the Debye length of the shell material. Recently, sensing mechanisms using C–S nanofibers[23] and C–S nanowires[24] were thoroughly investigated. From these studies, it was found that the radial modulation of the electron-depleted shell layer is the main factor in the improved sensing performance of these systems.

One important application of chemiresistive sensors that has recently emerged is the diagnosis of diseases by detecting disease markers in the exhaled breath of humans, which contains a number of volatile organic compounds (VOCs). This noninvasive diagnosis technique has advantages over other commonly used diagnosis methods, such as tomography or endoscopy. The information needed to diagnose a specific disease can be obtained from the detection of specific VOCs, which are known as biomarkers and have strong correlations with specific diseases.[25−29] A number of biomarkers in exhaled breath have been identified in previous studies;[30−40] hydrogen sulfide,[30,31] acetone,[32,33] toluene,[34,35] ammonia,[36−38] and carbon monoxide[39,40] are recognized biomarkers for halitosis, diabetes, lung cancer, kidney failure, and asthma, respectively.

However, the actual implementation of chemiresistive SMO NW sensors to diagnose specific diseases is still challenging because of their insufficient sensitivity to detect the extremely small variations of disease markers that exist in exhaled breath. In particular, despite the great improvement made to the reducing gas-sensing properties of SnO_2–ZnO C–S NWs[24] that were recently developed by the current authors, the sensitivity of the pristine C–S NWs is insufficient to be applied to the diagnosis of specific diseases.

One approach to improve the sensing properties of C–S structures even further is to expand the electron-depleted

Received: May 11, 2015
Accepted: July 22, 2015
Published: July 22, 2015

DOI: 10.1021/acsami.5b04066
ACS Appl. Mater. Interfaces 2015, 7, 17199−17208

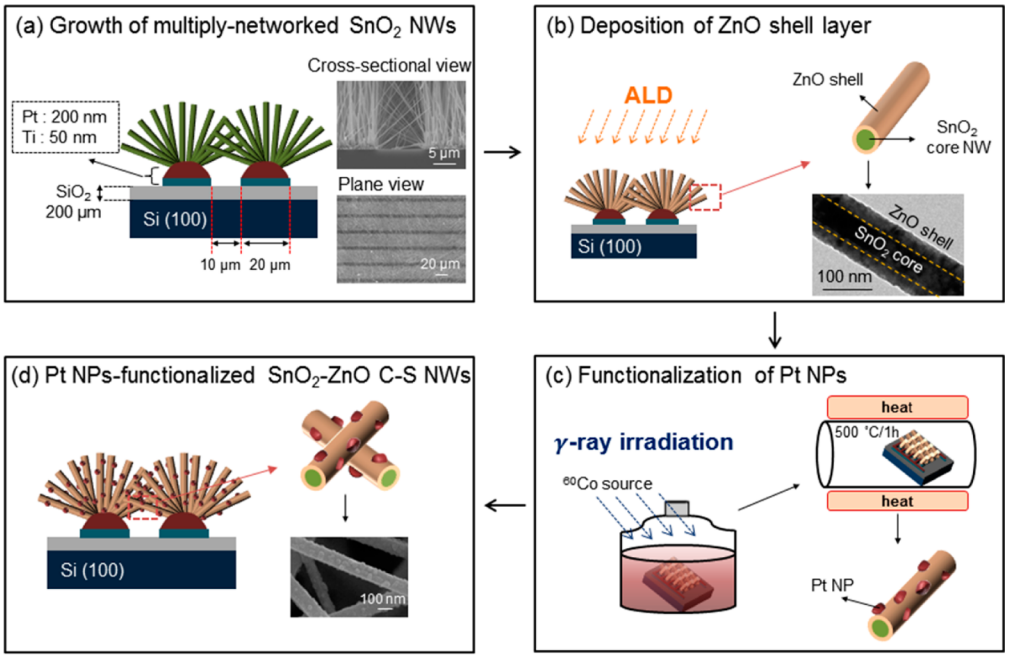

Figure 1. Schematic illustrations of the experimental procedures used to fabricate the Pt NP-functionalized SnO_2−ZnO C−S NWs. (a) The growth of highly networked SnO_2 NWs via the VLS method. (b) The deposition of ZnO shell layers with ALD. (c) The functionalization of the C−S NWs with Pt NPs by γ-ray radiolysis. (d) The resulting Pt NP-functionalized SnO_2−ZnO C−S NWs.

region in the shell layer, which is expected to produce larger resistance modulations during the gas adsorption and desorption processes. The attachment of metal nanoparticles (NPs) to the shell layer can cause electrons to flow from the shell layer to the attached metal NPs when the Fermi level of the metal NPs is lower than that of the shell layer. This flow of electrons will decrease the shell layer's electron density, which will increase the resistance modulation. In addition, if the metal used for the NPs can act as a catalyst for a specific gas, the catalytic sensitization will improve the sensing properties even further.

In this work, Pt NPs were attached to SnO_2−ZnO C−S NWs to increase the electron-depletion layer of the ZnO shell layer and add catalytic sensitization to the NWs through the catalytic effect of Pt on toluene (C_7H_8). With this novel approach, we realized the extraordinarily high sensitivity of 279 for 100 ppb of C_7H_8, which is the highest C_7H_8 sensitivity to be reported in the literature. The comprehensive review[41] regarding a new noninvasive and potentially inexpensive diagnosis of cancer relying on the detection of volatile organic compounds (VOCs) in exhaled breath provides a list of 115 validated cancer-related VOCs published in the literature during the past decade. It also classifies the cancer-related VOCs with respect to their "fat-to-blood" and "blood-to-air" partition coefficients. According to the review, C_7H_8 is indicative of lung cancer, though it cannot serve as a stand-alone biomarker of the disease. The Pt-functionalized C−S NWs developed in this work have great potential as the sensing platform in exhaled breath sensors that can be used to detect ppb-scale C_7H_8, which is one of the cancer-related VOCs.

2. EXPERIMENTAL METHODS

Fabrication of Highly Networked SnO_2−ZnO C−S NWs. The highly networked SnO_2−ZnO C−S NWs were synthesized in two steps. For the first step, a network of SnO_2 NWs was grown on a catalytic Au pad with the vapor−liquid−solid (VLS) method by evaporating a source of Sn. To form the networked NWs, a patterned interdigital electrode (PIE) was created with a conventional photolithographic process on a SiO_2 layer (200 nm thick) grown on Si (100) substrates. The trilayer PIE consisted of Au (3 nm thick), Pt (200 nm thick), and Ti (50 nm thick) layers, which were sequentially deposited with a sputtering method. The details of the fabricated PIEs were as follows: The total number of electrode pads was 20, each electrode pad was 1.05 mm long and 20 μm wider, and the gap between the adjacent electrode pads was 10 μm. The growth of the SnO_2 NWs was carried out in a horizontal quartz tube furnace at 900 °C for 15 min with N_2 and O_2 gases flowing at rates of 300 and 10 sccm, respectively. The SnO_2 NWs selectively grown on the PIE became entangled in the areas between the electrode's digits, which produced the networked junctions. This feature is illustrated in Figure 1a, in which actual cross-sectional and plane-view images are included. Both the experimental procedure for fabricating the networked SnO_2 nanowires and the effects of the length and diameter of the NWs on the gas-sensing properties were described in detail in an earlier paper.[42]

For the second step, atomic layer deposition (ALD) was used to coat the networked SnO_2 NWs with ZnO shells, which is a particularly effective fabrication technique for making a uniform, conformal layer on an irregularly shaped surface or object. For the ALD process, diethylzinc ($Zn(C_2H_5)_2$, DEZn) and H_2O were used as the precursors. For the ALD process, the temperature and pressure of the reactor were set at 150 °C and 0.3 Torr, respectively. One cycle of the ALD process had a DEZn dose time of 0.12 s, 3 s of purging with N_2, a H_2O dose time of 0.15 s, and, finally, 3 s of purging with N_2. By altering the number of ALD cycles, the thickness of the ZnO shells was successfully controlled to range from 5 to 80 nm. The experimental procedure for the ALD process is described in more detail in the literature.[24] A schematic of the fabrication process and a representative transmission electron microscopy (TEM) image of the SnO_2−ZnO C−S NWs are shown in Figure 1b. As can be seen, the uniform ZnO shell coating the SnO_2−ZnO C−S NWs has a thickness of 40 nm.

To compare sensing properties, sensors based on ZnO NWs were also prepared. The experimental procedure for the synthesis and fabrication of the ZnO NW sensors was similar to that used for the SnO_2 NWs sensors. The experimental conditions for fabricating the ZnO NWs are described in detail in one of our previous papers.[43]

DOI: 10.1021/acsami.5b04066
ACS Appl. Mater. Interfaces 2015, 7, 17199−17208

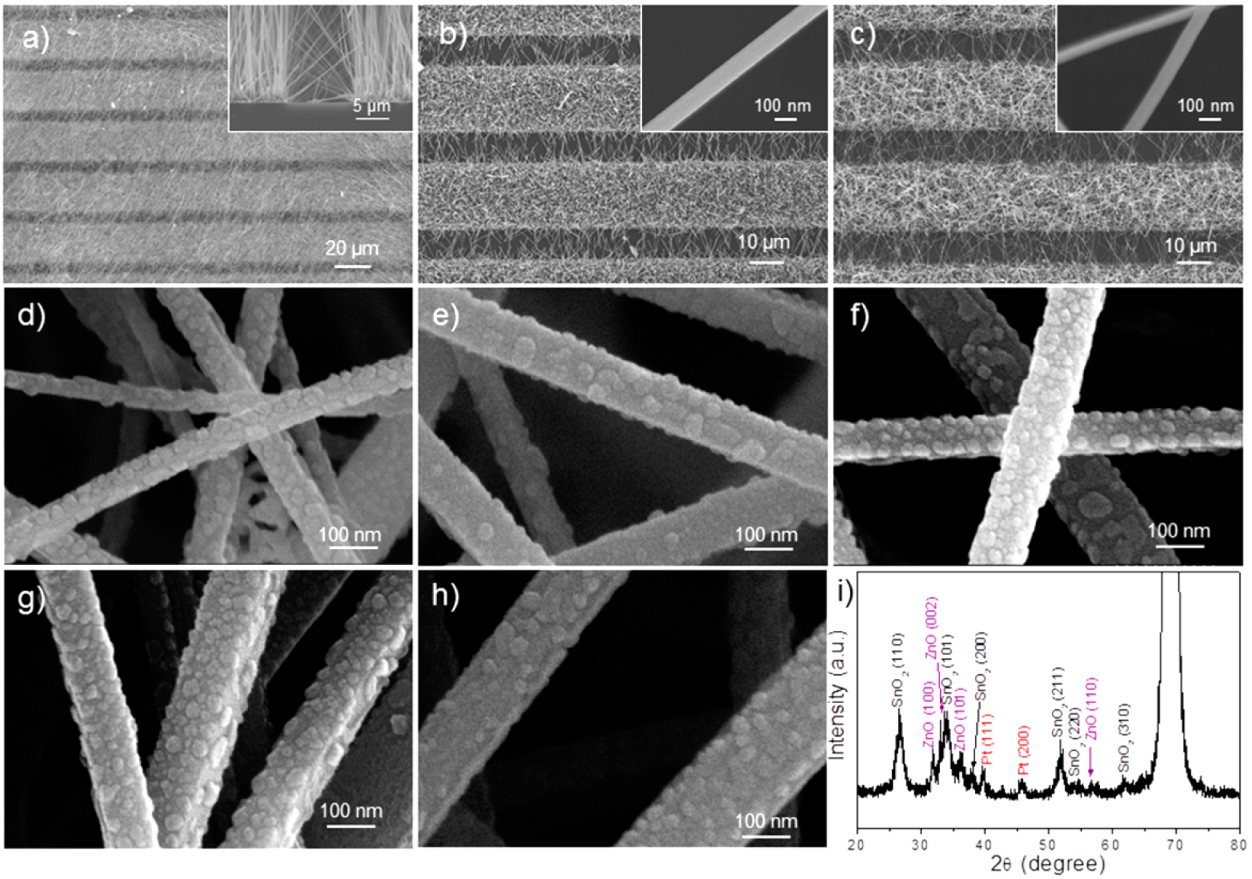

Figure 2. Typical plane-view FE-SEM images of the (a) pristine SnO_2 NWs, (b) pristine ZnO NWs, and (c) SnO_2−ZnO C−S NWs. The insets are the corresponding cross-sectional images. (d−h) Microstructures of the Pt NP-functionalized SnO_2−ZnO C−S NWs with 5, 10, 20, 50, and 80 nm thick shells, respectively. (i) A representative XRD pattern of the Pt NP-functionalized SnO_2−ZnO C−S NWs with a ZnO shell thickness of 80 nm.

Functionalization of the NWs with Pt NPs via γ-ray Radiolysis. The Pt NPs were synthesized and attached to the SnO_2−ZnO C−S NWs with the γ-ray radiolysis technique. The precursor solution was 1.0 mM of hydrogen hexachloroplatinate (IV) hydrate ($H_2PtCl_6 \cdot nH_2O$, n = 5.8, Kojima Chemicals Co.) dissolved in a mixture of deionized water (94 vol %) and 2-propanol (6 vol %). As illustrated in Figure 1c, the SnO_2−ZnO C−S NWs were immersed in the precursor solution and then exposed to ^{60}Co γ-rays in air under ambient conditions. This was performed at the Korea Atomic Energy Research Institute (KAERI). The γ-ray exposure conditions were an exposure time of 2 h and an illumination intensity of 10 $kGy \cdot h^{-1}$. The experimental procedure for the γ-ray radiolysis technique is described in detail in one of our previous papers.[44]

In Figure 1d, a real image of the resulting Pt NP-functionalized SnO_2−ZnO C−S NWs is shown, which demonstrates the uniform distribution of NPs on the surface of the C−S NWs.

Materials Characterization and Measuring the Sensing Performance. The microstructure of the synthesized samples was observed with field-emission scanning electron microscopy (FE-SEM). The detailed crystal structure, microstructure, and chemical composition were examined with X-ray diffraction (XRD), TEM, and energy-dispersive X-ray spectroscopy (EDS).

The C_7H_8-sensing performance of the Pt NP-functionalized C−S NWs was investigated as a function of the ZnO shell thickness. The cross-sensitivity of the sensors was evaluated with various reducing gases, such as carbon monoxide (CO), carbon dioxide (CO_2), and benzene (C_6H_6). The sensing measurements were carried out at 300 °C with a sensing measurement system after preliminary experiments were performed to determine the optimal operating temperature. The experimental procedure for the sensing measurements is described in detail in one of our earlier papers.[45] The response for the gases tested was evaluated with the relationship R_a/R_g, where R_a and R_g are the resistances in the absence and presence of an analyte gas, respectively.

3. RESULTS AND DISCUSSION

As demonstrated in Figure 2, a highly networked volume of SnO_2 NWs can be attained by using a deliberately designed PIE, which is further confirmed by the plane-view and cross-sectional (inset) FE-SEM images shown in Figure 2a. These images reveal the level of entanglement of the SnO_2 NWs, which can aid the chemiresistive electrical transport. According to our recent report,[42] chemical gas-sensing properties of SnO_2 networked NWs are likely to be associated with the nature of networking, particularly with the density of junctions. As the density of junctions increased, superior sensing properties were shown. One approach to obtain a larger density of junctions is to control the shape of nanowires; slender and long nanowires are more favorable. The other approach is to control the configuration of catalytic electrode layers, that is, PIEs. PIEs with a narrow distance and large pad area are more favorable. On the basis of these results, the SnO_2 NWs in this work were grown on the optimized PIE geometry.

On these networked SnO_2 NWs ZnO shell layers of various thicknesses were then deposited via ALD. Figure 2b shows the typical microstructure of the SnO_2−ZnO C−S NWs with a shell thickness of 20 nm. According to the plane-view image, the networked nature is maintained after the formation of the ZnO shell layer. The inset figure clearly shows that the ALD process results in the formation of uniform and conformal ZnO shell layers on the core SnO_2 NWs. For comparison purposes,

DOI: 10.1021/acsami.5b04066
ACS Appl. Mater. Interfaces 2015, 7, 17199−17208

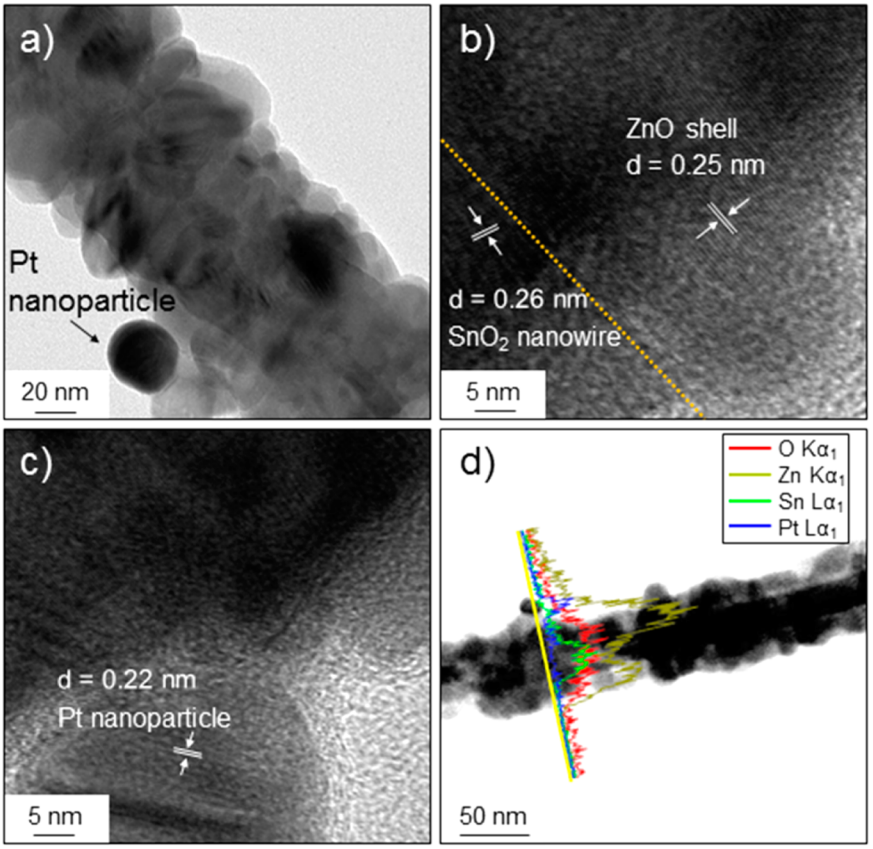

Figure 3. TEM images of the Pt NP-functionalized SnO_2−ZnO C−S NWs with a ZnO shell thickness of 50 nm. (a) A low-magnification TEM image. (b, c) High-resolution lattice images. (d) EDS line profiles for O, Sn, Zn, and Pt.

the microstructure of pristine ZnO NWs is shown in Figure 2c. The average diameter of the pristine ZnO NWs is approximately 70 nm.

The Pt NPs were synthesized and attached to the SnO_2−ZnO C−S NWs with various shell thicknesses via γ-ray radiolysis, and the resulting microstructures for shell thicknesses of 5, 10, 20, 50, and 80 nm are shown in Figure 2d−h, respectively. As can be seen, the Pt NPs, which are approximately 35 nm in diameter, are uniformly distributed on the C−S NWs, confirming that γ-ray radiolysis is an effective technique for creating metal NPs on metal oxide NWs.

XRD was used to identify the phases of the Pt-functionalized SnO_2−ZnO C−S NWs. A typical XRD pattern for the sample with a ZnO shell thickness of 50 nm is shown in Figure 2i. The XRD pattern, which was recorded with Cu Kα (1.5418 Å) radiation, shows that the Pt-functionalized SnO_2−ZnO C−S NWs are composed of SnO_2, ZnO, and Pt phases. The SnO_2 tetragonal rutile phase has lattice parameters of a = 4.73 Å and c = 3.18 Å (JCPDS card No. 88-0287), whereas the wurtzite phase of ZnO has lattice parameters of a = 3.24 Å and c = 5.205 Å (JCPDS card No. 89-0511). This XRD pattern is further evidence of the successful synthesis of Pt-functionalized SnO_2−ZnO C−S NWs. We have also estimated the size of Pt NPs using the Scherrer equation, $D = 0.89\{\lambda/(\beta \cos \theta)\}$, where D is the mean grain size, λ is the wavelength of X-rays (λ = 0.154 nm for Cu Kα radiation), and β is the full width at half-maximum of the diffraction peak at 2θ. The calculated value was 15.9 nm. Although this is smaller than the size (35 nm) estimated by the SEM image, the difference is acceptable considering the error that can be incorporated in the process of fitting the XRD peak.

The microstructure of the samples was further investigated with TEM. Figure 3 shows TEM images of the sample with a shell thickness of 50 nm. The low-magnification TEM image (Figure 3a) reveals the rugged nanometer-scale surface of the C−S NWs, with the Pt NPs strongly attached to the shell's surface. The high-resolution lattice images shown in Figure 3b,c confirm the purity of the phases in the SnO_2−ZnO C−S NWs and Pt NPs. The elemental mapping results for O, Sn, Zn, and Pt are displayed in Figure 3d. Although it is difficult to discuss the spatial distribution of each element with these profiles, the definite presence of each element supports the formation of Pt-functionalized SnO_2−ZnO C−S NWs.

The C_7H_8-sensing performance of the Pt-functionalized SnO_2−ZnO C−S NW sensors with various shell thicknesses was investigated, with the results shown in Figure 4. For comparison purposes, the sensing performance of sensors fabricated from pristine SnO_2 NWs, pristine ZnO NWs, and SnO_2−ZnO C−S NWs with various shell thicknesses was measured and is shown in Figure 4a−c, respectively. All the sensors clearly track the changing C_7H_8 concentration in the environment. The resistance of the sensors decreases as the C_7H_8 is supplied and then increases once the flow of C_7H_8 is stopped. This behavior can be explained by the well-known n-type semiconductor sensing mechanism, which is outlined in the following sentences. In ambient air, the adsorption of oxygen species onto the surface of the NWs results in the capture of electrons in the conduction band of the NWs. This creates an electron-depleted region underneath the surface of

DOI: 10.1021/acsami.5b04066
ACS Appl. Mater. Interfaces 2015, 7, 17199−17208

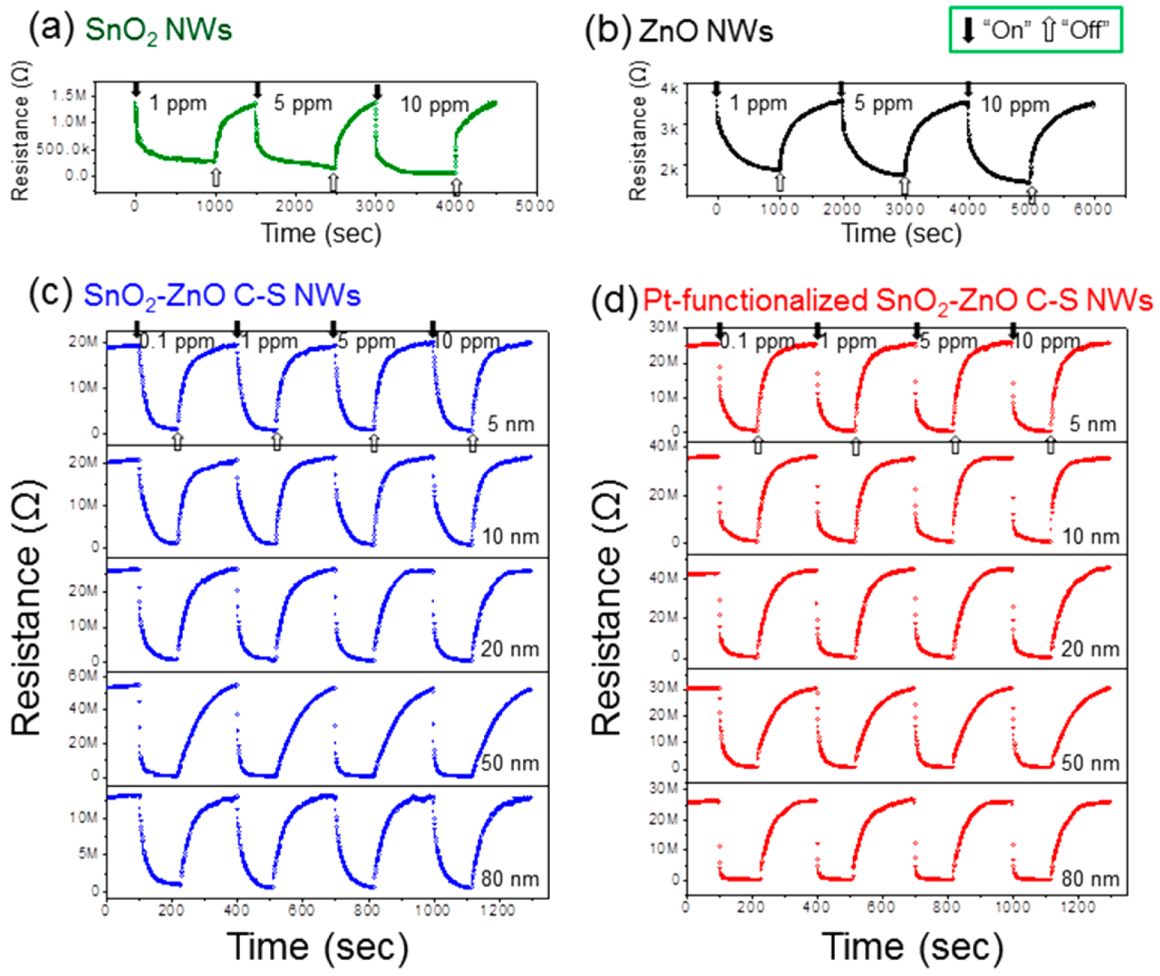

Figure 4. Dynamic resistance curves of the (a) SnO_2 NWs, (b) ZnO NWs, (c) SnO_2−ZnO C−S NWs, and (d) Pt NP-functionalized SnO_2−ZnO C−S NWs for a varying concentration of C_7H_8.

the NWs, which radially suppresses the charge-carrier conduction channels along the NWs' length. When the reducing gas molecules are introduced, they usually interact with the adsorbed oxygen species, forming chemical species that desorb from the surface of the NWs, releasing the captured electrons back into the conduction band. This decreases the electron-depleted region, leading to a decrease in resistance, which is the source of the resistance modulation observed in the NW samples tested in this work. One important feature of Figure 4 is that the sensor response is highly dependent on the shell thickness.

To visualize the differences between the C_7H_8 responses clearly, the responses of the samples to 100 ppb of C_7H_8 are summarized in Figure 5. The responses of pristine SnO_2 and ZnO NWs are 1.8 and 1.16 for 1 ppm of C_7H_8, respectively; they did not show any meaningful resistance modulation for 100 ppb of C_7H_8. By creating the ZnO shell layer on the pristine SnO_2 NWs, the C_7H_8 response greatly increases up to 73 as the shell thickness increases up to 50 nm. As the shell thickness increases further, the C_7H_8 response decreases. This bell-shaped response curve to a reducing gas as a function of the shell thickness was explained in our previous paper.[24] As can be seen in Figure 5, the C_7H_8 response is further improved by the Pt functionalization. The response increases proportionally with increasing shell thickness, with the Pt-functionalized SnO_2−ZnO C−S NWs with a shell thickness 80 nm

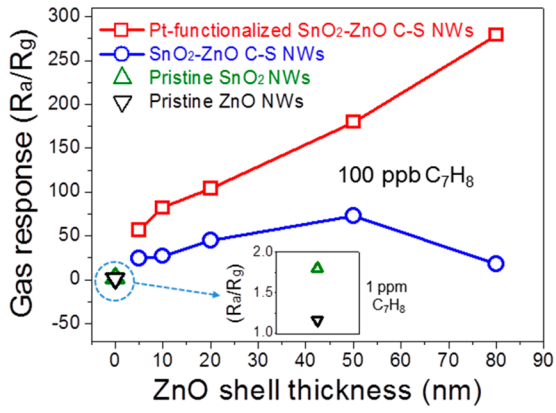

Figure 5. Responses of the SnO_2−ZnO C−S NWs with and without Pt NPs as a function of the ZnO shell thickness for 100 ppb of C_7H_8. For comparison purposes, the responses of the pristine SnO_2 and ZnO NWs for 1 ppm of C_7H_8 are included because they could not detect 100 ppb of C_7H_8.

showing a response of 279 for 100 ppb of C_7H_8. To the best of our knowledge, this is the highest response to be reported in the literature and is sufficient for use in exhaled breath sensors for detecting ppb-scale C_7H_8. In Table 1, the C_7H_8 responses of the various NWs tested in this work are compared to those reported in the literature. By considering the C_7H_8 concen-

DOI: 10.1021/acsami.5b04066
ACS Appl. Mater. Interfaces 2015, 7, 17199−17208

Table 1. Comparison of the C_7H_8-Sensing Responses of the Pt-Functionalized SnO_2−ZnO C−S NWs in This Work to That Reported in the Literature

material type	C_7H_8 concentration (ppm)	response (R_a/R_g)	temp (°C)	ref
ZnO C−S hollow microspheres	20	24.5	300	46
Au-functionalized ZnO nanowires	1	<2.5	340	47
Co_3O_4 nanorods	200	35	200	48
NiO−SnO_2 composite nanofibers	50	11	330	49
TiO_2-doped flowerlike ZnO nanostructures	1	1.9	290	50
SnO_2 nanofibers	200	9	350	51
nanostructured films composed of TiO_2 nanotubes	50	25	500	52
Co_3O_4 hollow nanospheres	10	3	100	53
ZnO−SnO_2 composite nanofibers	100	9.8	360	54
ZnO nanowires	1	1.16	300	this work
SnO_2 nanowires	1	1.8	300	this work
SnO_2−ZnO C−S nanowires (shell thickness = 50 nm)	0.1	73	300	this work
Pt-functionalized SnO_2−ZnO C−S nanowires (shell thickness = 80 nm)	0.1	279	300	this work

tration and corresponding response, it is reasonable to claim that the Pt-functionalized SnO_2−ZnO C−S NWs have an outstanding response to trace concentrations of C_7H_8.

Selectivity is an important parameter that must be fulfilled for the practical implementation of sensors. In principle, selectivity of a specific analyte can be claimed only when one has a mixture that includes the targeted analyte, and from there, one can make the required detection of the targeted analyte. In this work, for a qualitative evaluation to C_7H_8-selective sensing properties of the Pt-functionalized SnO_2−ZnO C−S NWs, the C−S NWs with a shell thickness 80 nm were tested with common reducing gases, such as CO, CO_2, and C_6H_6. Note that they are not a mixture gas but a separate gas diluted in air. Figure 6a shows the dynamic resistance curves for various concentrations of the tested reducing gases, and the sensor responses are summarized in Figure 6b. As can be seen, the response to C_7H_8 is approximately 2.5 times higher than those to the other reducing gases, which demonstrates that the Pt-functionalized SnO_2−ZnO C−S NWs are likely to have a good selective detection for sub-ppm concentrations of C_7H_8. The exact selectivity of the samples needs to perform with a mixture gas in the next stage work.

The improved C_7H_8-sensing abilities of the SnO_2−ZnO C−S NWs without the Pt NPs compared to the pristine SnO_2 NWs are attributed to the intensified radial modulation of the electron-depleted region in the shell layer. The modulation of the resistance appears to be maximized at a specific thickness (Figure 5). As Figure 7 illustrates, in ambient air, an electron-depleted shell layer is established because of the adsorption of oxygen species onto the *n*-type ZnO shell and the C−S heterojunction formation. The energy band diagrams included in Figure 7 explain the electron flow at the heterointerface between the ZnO and SnO_2. When C_7H_8 gas is present, the captured electrons return to the conduction band of ZnO, reducing the level of electron depletion in the shell layer. The degree of resistance modulation originating from this radial modulation of the electron-depleted shell layer varies according to the shell thickness; a thinner shell exhibits a more pronounced resistance modulation, while a thicker shell exhibits less resistance modulation because the shell is only partially depleted. As illustrated in the lower part of Figure 7, in addition to this radial modulation, we need to consider another contribution: the fraction of the total volume of the C−S NWs corresponding to the shell layers. This fraction is proportional to the shell thickness, and therefore, the combined

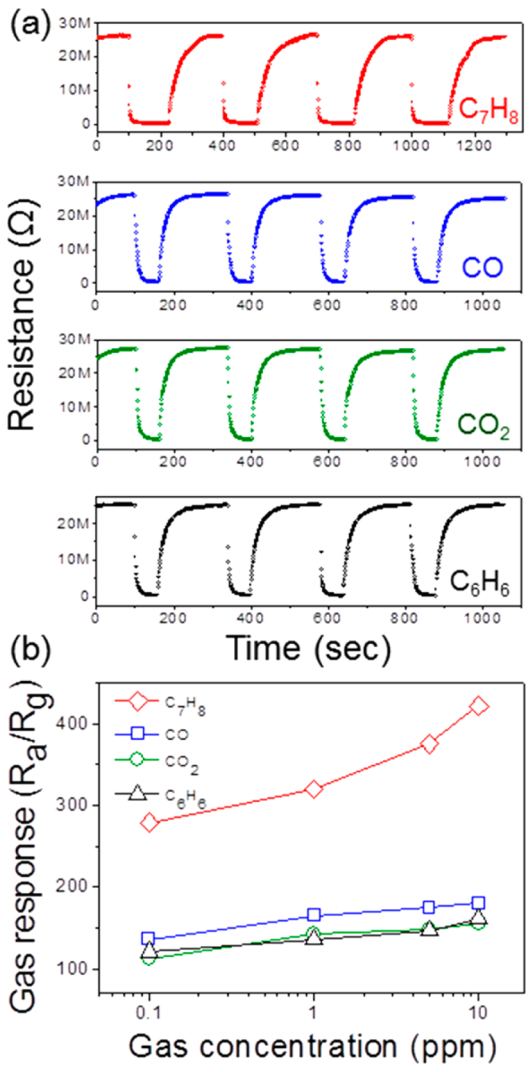

Figure 6. (a) Dynamic resistance curves of the Pt NP-functionalized SnO_2−ZnO C−S NWs with a ZnO shell thickness of 80 nm for C_7H_8, CO, CO_2, and C_6H_6. (b) A summary of the gas responses.

total response to a reducing gas can be depicted as a bell-shaped curve with respect to the shell thickness. This is in good agreement with the C_7H_8-sensing behavior observed for the SnO_2−ZnO C−S NWs, with the results showing that a 50 nm thick shell has the best C_7H_8-sensing ability. Note that the

DOI: 10.1021/acsami.5b04066
ACS Appl. Mater. Interfaces 2015, 7, 17199−17208

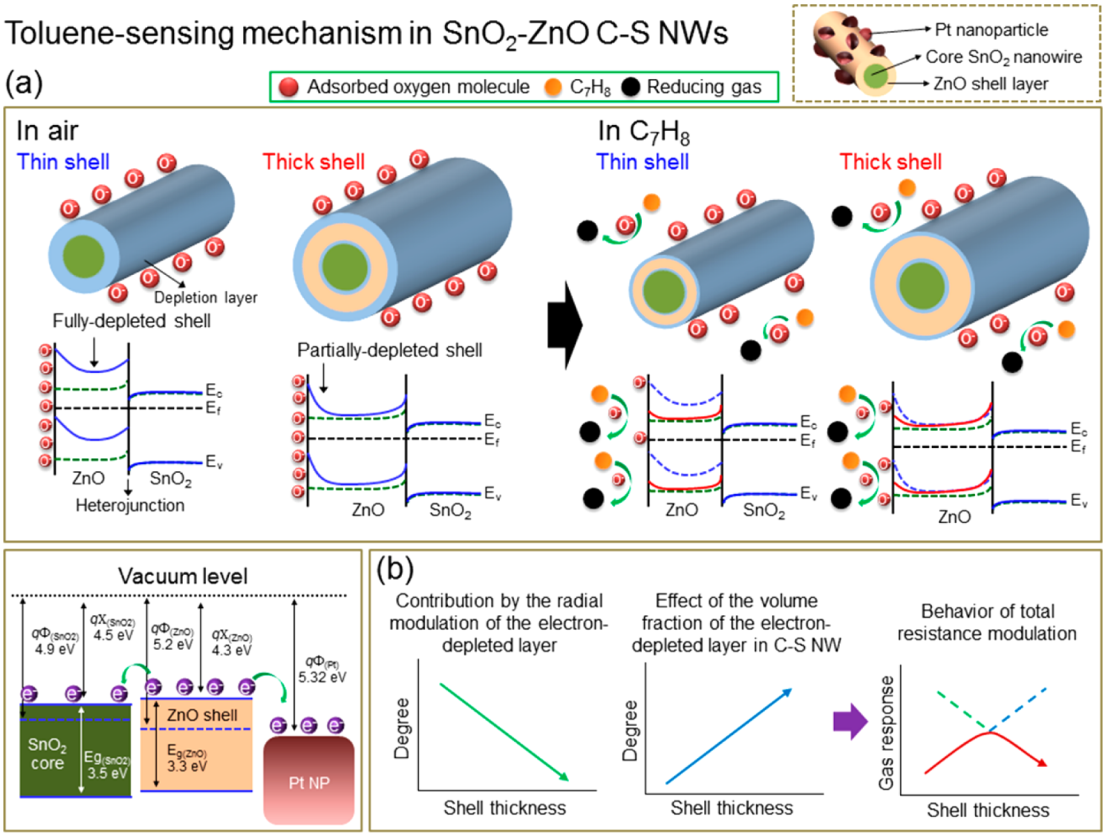

Figure 7. Schematics illustrating the C_7H_8-sensing mechanisms of the pristine SnO_2–ZnO C–S NWs. (a) The resistance modulation due to the radial modulation of the electron-depleted region in the shell layer. (b) The resistance modulation contributed by the fraction of the total volume of the C–S NWs corresponding to the shell layers, which is proportional to the shell thickness, resulting in the bell-shaped curve.

electric field smearing effect mentioned in the earlier work[24] may still exist in the thin shell of C–S NWs after its functionalization with Pt NPs, but cannot be deconvoluted from other contributions.

The functionalization with Pt NPs introduces two additional contributions to the sensing properties of the SnO_2–ZnO C–S NWs. One contribution is the electronic sensitization (ES) that originates from the flow of electrons from the ZnO shell layer to the Pt NPs, leading to the additional suppression of the conduction channels created inside the ZnO shell layer. The energy band diagrams are shown in the lower part of Figure 7. The expansion of the electron-depleted region in the shell layer consequently intensifies the resistance modulation of the SnO_2–ZnO C–S NWs when C_7H_8 molecules interact with the adsorbed oxygen species. The other contribution is the chemical sensitization (CS) from the catalytic effect of the Pt NPs, which facilitates more interactions between the C_7H_8 and adsorbed oxygen species, increasing the resistance modulation of the SnO_2–ZnO C–S NWs. These ES and CS effects are described in Figure 8a. The size of the ES contribution is likely to be solely dependent on the metal used for the NPs, and therefore, the CS contribution is mainly responsible for the selective detection because of the different degrees of catalytic interaction between the metal NPs and a specific gas. As illustrated in Figure 8b, because of the ES and CS contributions of the Pt NPs, the response of the Pt-functionalized SnO_2–ZnO C–S NWs is further increased and the maximum response shifts toward a thicker shell. As shown in Figure 5, in contrast to the SnO_2–ZnO C–S NWs without the Pt NPs, the response of the Pt-functionalized SnO_2–ZnO C–S NWs linearly increases with increasing shell thickness. This is because the maximum response shifts toward a thicker shell and we did not test a shell thick enough to reach the maximum response. In the literature, there are some studies regarding the application of Pt to enhance the gas-sensing properties of SMOs.[55,56] However, it is currently not clear why the Pt NPs are more effective at enhancing the sensing behavior of the SnO_2–ZnO C–S NWs with respect to C_7H_8 gas than the other reducing gases tested. Therefore, we surmise that the Pt NPs may dissociate the C_7H_8 gas more effectively than the other gases tested (i.e., CO, CO_2, and C_6H_6.). C_7H_8, among the gases tested, is unique since it has an additional methyl group ($-CH_3$). This group plays a crucial role in enhancing the sensitivity of sensors.[57] The adsorption of C_7H_8 onto the Pt surface is significantly affected by electronic effects,[58] which lower the barrier for adsorption of C_7H_8 by making the donation of electrons from the π_{CH_3} level to the Fermi level easier and by the making back-donation from the Fermi level to the $\pi_{CH_3^*}$ level more facile. The effect of Pt on the NWs' performance can be revealed by Kelvin probe measurements,[59] which will be a future research work.

The performance of gated Si NW gas sensors, emerging as promising devices for chemical and biological sensing applications, is usually accompanied by a "hysteresis" phenomenon, which limits their performance under real world conditions.[59] The hysteresis in the Si NW field effect transistor (FET) is caused by surface trap sites. In contrast, the Pt-functionalized C–S NWs of the current study are not the sensor device operating in the frame of FET, but chemir-

DOI: 10.1021/acsami.5b04066
ACS Appl. Mater. Interfaces 2015, 7, 17199–17208

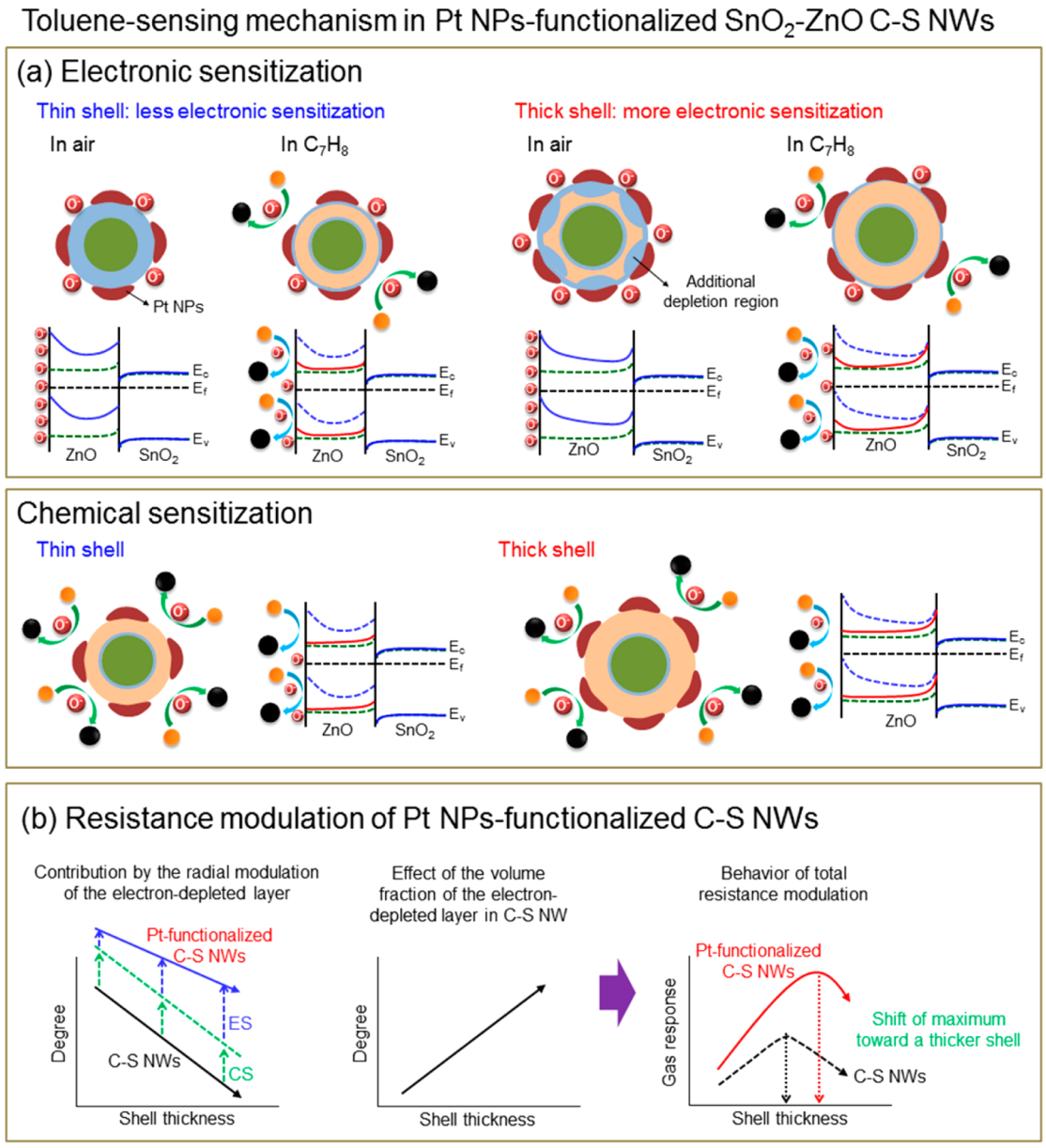

Figure 8. Schematics illustrating the C_7H_8-sensing mechanisms of the Pt NP-functionalized SnO_2−ZnO C−S NWs. (a) The ES and CS effects of the Pt NPs. (b) The increased C_7H_8 response and shift of the maximum response toward a thicker shell because of the effects of the Pt NPs.

esistive-type sensors. Moreover, they operate at a higher temperature, 300 °C, meaning that the influence of surface trap sites that are a major origin of the hysteresis can be excluded. In this sense, there is no need of considering the hysteresis in the Pt-functionalized C−S NWs.

One of the major issues of chemiresist-type sensors is the effect of humidity on the sensing performance. The sensitivity of sensors is dependent on the relative humidity in the atmosphere.[60−62] In general, the adsorption of water vapor to the metal oxide surface will lower the sensitivity of metal oxide sensors because it may not only induce a decrease in baseline resistance of the gas sensor but also lead to less chemisorption of oxygen species in air.[61] Furthermore, prolonged exposure to humid environments may lead to the gradual formation of stable chemisorbed OH^- on the surface,[60] causing a progressive deterioration of the sensitivity of gas sensors. Further investigation on the effect of humidity is required for a more precise evaluation for the sensing values obtained from the Pt-functionalized C−S NWs.

4. CONCLUSIONS

Exceptionally high C_7H_8-sensing properties were realized with networked SnO_2−ZnO C−S NWs functionalized with Pt NPs. This sensing platform achieved a sensitivity of 279 for 100 ppb of C_7H_8, which is the highest toluene sensitivity to be reported in the literature. The combined effects of the expanded electron-depleted region in the shell layer and the catalytic role of the functionalized Pt NPs are responsible for the outstanding C_7H_8 sensitivity and selectivity. This novel approach of using networked C−S NWs functionalized with noble metal NPs may pave the way for the development of extremely sensitive and selective chemiresistive chemical gas sensors that can be applied to exhaled breath sensors used for the diagnosis of diseases.

DOI: 10.1021/acsami.5b04066
ACS Appl. Mater. Interfaces 2015, 7, 17199−17208

AUTHOR INFORMATION

Corresponding Author

*E-mail: sangsub@inha.ac.kr.

Author Contributions

S.S.K. conceived the study, designed the experiments, and prepared the manuscript. J.-H.K. performed the experiments. Both authors have given approval to the final version of the manuscript.

Notes

The authors declare no competing financial interest.

ACKNOWLEDGMENTS

This work was supported by Inha University.

REFERENCES

(1) Kwon, O. S.; Park, S. J.; Yoon, H.; Jang, J. Highly Sensitive and Selective Chemiresistive Sensors Based on Multidimensional Polypyrrole Nanotubes. *Chem. Commun.* **2012**, *48*, 10526−10528.

(2) Penza, M.; Cassano, G.; Rossi, R.; Rizzo, A.; Signore, M. A.; Alvisi, M.; Lisi, N.; Serra, E.; Girogi, R. Effect of Growth Catalysts on Gas Sensitivity in Carbon Nanotube Film Based Chemiresistive Sensors. *Appl. Phys. Lett.* **2007**, *90*, 103101.

(3) Wan, Q.; Li, Q. H.; Chen, Y. J.; Wang, T. H.; He, X. L.; Li, J. P.; Lin, C. L. Fabrication and Ethanol Sensing Characteristics of ZnO Nanowire. *Appl. Phys. Lett.* **2004**, *84*, 3654−3656.

(4) Choi, S.-W.; Katoch, A.; Sun, G.-J.; Kim, S. S. Bimetallic Pd/Pt Nanoparticle-Functionalized SnO_2 Nanowires for Fast Response and Recovery to NO_2. *Sens. Actuators, B* **2013**, *181*, 446−453.

(5) Park, S.; Ko, H.; Kim, S.; Lee, C. Role of the Interfaces in Multiple Networked One-Dimensional Core-Shell Nanostructured Gas Sensors. *ACS Appl. Mater. Interfaces* **2014**, *6*, 9595−9600.

(6) Katoch, A.; Choi, S.-W.; Sun, G.-J.; Kim, S. S. Low Temperature Sensing Properties of Pt Nanoparticle-Functionalized Networked ZnO Nanowires. *J. Nanosci. Nanotechnol.* **2015**, *15*, 330−333.

(7) Park, S.; An, S.; Ko, H.; Lee, C. Fabrication, Structures, and Gas Sensing of Multiple-Networked Pt-Functionailzed Bi_2O_3 Nanowires. *J. Nanosci. Nanotechnol.* **2015**, *15*, 1605−1609.

(8) Sun, G.-J.; Choi, S.-W.; Katoch, A.; Wu, P.; Kim, S. S. Bi-Functional Mechanism of H_2S Detection Using Cuo-SnO_2 Nanowires. *J. Mater. Chem. C* **2013**, *1*, 5454−5462.

(9) Choi, S.-W.; Jung, S.-H.; Kim, S. S. Functionalization of Selectively Grown Networked SnO_2 Nanowires with Pd Nanodots by Gamma-Ray Radiolysis. *Nanotechnology* **2011**, *22*, 225501.

(10) Choi, S.-W.; Katoch, A.; Kim, J.-H.; Kim, S. S. A Novel Approach to Improving Oxidizing Gas Sensing Ability of p-CuO Nanowires Using Biased Radial. *J. Mater. Chem. C* **2014**, *2*, 8911−8917.

(11) Kim, J.-H.; Katoch, A.; Choi, S.-W.; Kim, S. S. Growth and Sensing Properties of Networked p-CuO Nanowires. *Sens. Actuators, B* **2015**, *212*, 190−195.

(12) Park, J. Y.; Choi, S.-W.; Kim, S. S. Tailoring the Number of Junctions per Electrode Pair in Networked ZnO Nanowire Sensors. *J. Am. Ceram. Soc.* **2011**, *94*, 3922−3926.

(13) Choi, S.-W.; Kim, S. S. Room Temperature CO Sensing of Selectively Grown Networked ZnO Nanowires by Pd Nanodot Functionalization. *Sens. Actuators, B* **2012**, *168*, 8−13.

(14) Singh, N.; Ponzoni, A.; Gupta, R. K.; Lee, P. S.; Comini, E. Synthesis of In_2O_3−ZnO Core−Shell Nanowires and Their Application in Gas Sensing. *Sens. Actuators, B* **2011**, *160*, 1346−1351.

(15) Jang, Y.-G.; Kim, W.-S.; Kim, D.-H.; Hong, S.-H. Fabrication of Ga_2O_3/SnO_2 Core−Shell Nanowires and Their Ethanol Gas Sensing Properties. *J. Mater. Res.* **2011**, *26*, 2322−2327.

(16) Chen, Y.-J.; Xiao, G.; Wang, T.-S.; Zhang, F.; Ma, Y.; Gao, P.; Zhu, C.-L.; Zhang, E.; Xu, Z.; Li, Q.-H. Synthesis and Enhanced Gas Sensing Properties of Crystalline CeO_2/TiO_2 Core/Shell Nanorods. *Sens. Actuators, B* **2011**, *156*, 867−874.

(17) Liu, X.; Zhang, J.; Guo, X.; Wang, S.; Wu, S. Core−Shell α−Fe_2O_3@SnO_2/Au Hybrid Structures and Their Enhanced Gas Sensing Properties. *RSC Adv.* **2012**, *2*, 1650−1655.

(18) Zhang, J.; Liu, X.; Wang, L.; Yang, T.; Guo, X.; Wu, S.; Wang, S.; Zhang, S. Synthesis and Gas Sensing Properties of α-Fe_2O_3@ZnO Core−Shell Nanospindles. *Nanotechnology* **2011**, *22*, 185501.

(19) Choi, S.-W.; Park, J. Y.; Kim, S. S. Synthesis of SnO_2−ZnO Core−Shell Nanofibers via a Novel Two-Step Process and Their Gas Sensing Properties. *Nanotechnology* **2009**, *20*, 465603.

(20) Rai, P.; Khan, R.; Raj, S.; Majhi, S. M.; Park, K.-K.; Yu, Y.-T.; Lee, I.-H.; Sekhar, P. K. Au@Cu_2O Core−Shell Nanoparticles as Chemiresistors for Gas Sensor Applications: Effect of Potential Barrier Modulation on the Sensing Performance. *Nanoscale* **2014**, *6*, 581−588.

(21) Park, J. Y.; Choi, S.-W.; Kim, S. S. A Model for the Enhancement of Gas Sensing Properties in SnO_2-Zno Core-Shell Nanofibers. *J. Phys. D: Appl. Phys.* **2011**, *44*, 205403.

(22) Katoch, A.; Choi, S.-W.; Sun, G.-J.; Kim, S. S. An Approach to Detecting a Reducing Gas by Radial Modulation of Electron Depleted Shells in Core-Shell Nanofibers. *J. Mater. Chem. A* **2013**, *1*, 13588−13596.

(23) Katoch, A.; Choi, S.-W.; Sun, G.-J.; Kim, H. W.; Kim, S. S. Mechanism and Prominent Enhancement of Sensing Ability to Reducing Gases in p/n Core−Shell Nanofibers. *Nanotechnology* **2014**, *25*, 175501.

(24) Choi, S.-W.; Katoch, A.; Sun, G.-J.; Kim, J.-H.; Kim, S.-H.; Kim, S. S. Dual Functional Sensing Mechanism in SnO_2-ZnO Core-Shell Nanowires. *ACS Appl. Mater. Interfaces* **2014**, *6*, 8281−8287.

(25) Wang, B.; Cancilla, J. C.; Torrecilla, J. S.; Haick, H. Artificial Sensing Intelligence with Silicon Nanowires for Ultraselective Detection in the Gas Phase. *Nano Lett.* **2014**, *14*, 933−938.

(26) Tung, T. T.; Castro, M.; Pillin, I.; Kim, T. Y.; Suh, K. S.; Feller, J.-F. Graphene−Fe_3O_4/PIL−PEDOT for the Design of Sensitive and Stable Quantum Chemo-Resistive VOC Sensors. *Carbon* **2014**, *74*, 104−112.

(27) Lee, I.; Choi, S.-J.; Park, K.-M.; Lee, S. S.; Choi, S.; Kim, I.-D.; Park, C. O. The Stability, Sensitivity and Response Transients of ZnO, SnO_2 and WO_3 Sensors under Acetone, Toluene and H_2S Environments. *Sens. Actuators, B* **2014**, *197*, 300−307.

(28) Sethi, S.; Nanda, R.; Chakraborty, T. 2013 Clinical Application of Volatile Organic Compound Analysis for Detecting Infectious Diseases. *Clin. Microbiol. Rev.* **2013**, *26*, 462−475.

(29) Itoh, T.; Nakashima, T.; Akamatsu, T.; Izu, N.; Shin, W. Nonanal Gas Sensing Properties of Platinum, Palladium, and Gold-Loaded Tin Oxide VOCs Sensors. *Sens. Actuators, B* **2013**, *187*, 135−141.

(30) Choi, S.-J.; Choi, C.; Kim, S.-J.; Cho, H.-J.; Hakim, M.; Jeon, S.; Kim, I.-D. Highly Efficient Electronic Sensitization of Non-Oxidized Graphene Flakes on Controlled Pore-Loaded WO_3 Nanofibers for Selective Detection of H_2S Molecules. *Sci. Rep.* **2015**, *5*, 8067.

(31) Liu, C.; Hayashi, K.; Toko, K. Au Nanoparticles Decorated Polyaniline Nanofiber Sensor for Detecting Volatile Sulfur Compounds in Expired Breath. *Sens. Actuators, B* **2012**, *161*, 504−509.

(32) Ye, M.; Chien, P.-J.; Toma, K.; Arakawa, T.; Mitsubayashi, K. An Acetone Bio-Sniffer (Gas Phase Biosensor) Enabling Assessment of Lipid Metabolism from Exhaled Breath. *Biosens. Bioelectron.* **2015**, *73*, 208−213.

(33) Choi, S.-J.; Lee, I.; Jang, B.-H.; Youn, D.-Y.; Ryu, W.-H.; Park, C. O.; Kim, I.-D. Selective Diagnosis of Diabetes Using Pt-Functionalized WO_3 Hemitube Networked as a Sensing Layer of Acetone in Exhaled Breath. *Anal. Chem.* **2013**, *85*, 1792−1796.

(34) Ju, S.; Lee, K.-Y.; Min, S.-J.; Yoo, Y. K.; Hwang, K. S.; Kim, S. K.; Yi, H. Single-Carbon Discrimination by Selected Peptides for Individual Detection of Volatile Organic Compounds. *Sci. Rep.* **2015**, *5*, 9196.

(35) Xing, R.; Xu, L.; Song, J.; Zhou, C.; Li, Q.; Liu, D.; Song, H. W. Preparation and Gas Sensing Properties of In_2O_3/Au Nanorods for Detection of Volatile Organic Compounds in Exhaled Breath. *Sci. Rep.* **2015**, *5*, 10717.

DOI: 10.1021/acsami.5b04066
ACS Appl. Mater. Interfaces 2015, 7, 17199−17208

(36) Righettoni, M.; Amann, A.; Pratsinis, S. E. Breath Analysis by Nanostructured Metal Oxides as Chemo-Resistive Gas Sensors. *Mater. Today* **2015**, *18*, 163−171.
(37) Agapiou, A.; Amann, A.; Mochalski, P.; Statheropoulos, M.; Thomas, C. L. P. Trace Detection of Endogenous Human Volatile Organic Compounds for Search, Rescue and Emergency Applications. *TrAC, Trends Anal. Chem.* **2015**, *66*, 158−175.
(38) Ogimoto, Y.; Selyanchyn, R.; Takahara, N.; Wakamatsu, S.; Lee, S.-W. Detection of Ammonia in Human Breath Using Quartz Crystal Microbalance Sensors with Functionalized Mesoporous SiO_2 Nanoparticle Films. *Sens. Actuators, B* **2015**, *215*, 428−436.
(39) Kwan, A. M.; Fung, A. G.; Jansen, P. A.; Schivo, M.; Kenyon, N. J.; Delplanque, J.-P.; Davis, C. E. Personal Lung Function Monitoring Devices for Asthma Patients. *IEEE Sens. J.* **2015**, *15*, 2238−2247.
(40) Evans, K. A.; Halterman, J. S.; Hopke, P. K.; Fagnano, M.; Rich, D. Q. Increased Ultrafine Particles and Carbon Monoxide Concentrations are Associated with Asthma Exacerbation Among Urban Children. *Environ. Res.* **2014**, *129*, 11−19.
(41) Haick, H.; Broza, Y. Y.; Mochalski, P.; Ruzsanyi, V.; Amann, A. Assessment, Origin, and Implementaton of Breath Volatile Cancer Markers. *Chem. Soc. Rev.* **2014**, *43*, 1423−1449.
(42) Park, J. Y.; Choi, S.-W.; Kim, S. S. Junction-Tuned SnO_2 Nanowires and Their Sensing Properties. *J. Phys. Chem. C* **2011**, *115*, 12774−12781.
(43) Park, J. Y.; Park, Y. K.; Kim, S. S. Formation of Networked ZnO Nanowires By Vapor Phase Growth and Their Sensing Properties with Respect to CO. *Mater. Lett.* **2011**, *65*, 2755−2757.
(44) Sun, G.-J.; Choi, S.-W.; Jung, S.-H.; Katoch, A.; Kim, S. S. V-Groove SnO_2 Nanowire Sensors Fabrication and Pt-Nanoparticle Decoration. *Nanotechnology* **2013**, *24*, 025504.
(45) Choi, S.-W.; Katoch, A.; Kim, J.-H.; Kim, S. S. Striking Sensing Improvement of n-Type Oxide Nanowires by Electronic Sensitization Based on Work Function Difference. *J. Mater. Chem. C* **2015**, *3*, 1521−1527.
(46) Wang, L.; Lou, Z.; Fei, T.; Zhang, T. Zinc Oxide Core−Shell Hollow Microspheres with Multi-Shelled Architecture for Gas Sensor Applications. *J. Mater. Chem.* **2011**, *21*, 19331−19336.
(47) Wang, L.; Wang, S.; Xu, M.; Hu, X.; Zhang, H.; Wang, Y.; Huang, W. A Au-Functionalized ZnO Nanowire Gas Sensor for Detection of Benzene and Toluene. *Phys. Chem. Chem. Phys.* **2013**, *15*, 17179−17186.
(48) Wang, L.; Deng, J.; Lou, Z.; Zhang, T. Nanoparticles-Assembled Co_3O_4 Nanorods p-Type Nanomaterials: One-Pot Synthesis and Toluene-Sensing Properties. *Sens. Actuators, B* **2014**, *201*, 1−6.
(49) Liu, L.; Zhang, Y.; Wang, G.; Li, S.; Wang, L.; Han, Y.; Jiang, X.; Wei, A. High Toluene Sensing Properties of Nio−SnO_2 Composite Nanofiber Sensors Operating at 330 °C. *Sens. Actuators, B* **2011**, *160*, 448−454.
(50) Zeng, Y.; Zhang, T.; Wang, L.; Kang, M.; Fan, H.; Wang, R.; He, Y. Enhanced Toluene Sensing Characteristics of TiO_2-Doped Flowerlike ZnO Nanostructures. *Sens. Actuators, B* **2009**, *140*, 73−78.
(51) Qi, Q.; Zhang, T.; Liu, L.; Zheng, X. Synthesis and Toluene Sensing Properties of SnO_2 Nanofibers. *Sens. Actuators, B* **2009**, *137*, 471−475.
(52) Seo, M.-H.; Yuasa, M.; Kida, T.; Huh, J.-S.; Shimanoe, K.; Yamazoe, N. Gas Sensing Characteristics and Porosity Control of Nanostructured Films Composed of TiO_2 Nanotubes. *Sens. Actuators, B* **2009**, *137*, 513−520.
(53) Park, J.; Shen, X.; Wang, G. Solvothermal Synthesis and Gas-Sensing Performance of Co_3O_4 Hollow Nanospheres. *Sens. Actuators, B* **2009**, *136*, 494−498.
(54) Song, X.; Zhang, D.; Fan, M. A Novel Toluene Sensor Based on ZnO−SnO_2 Nanofiber Web. *Appl. Surf. Sci.* **2009**, *255*, 7343−7347.
(55) Choi, S.-W.; Kim, S. S. Platinum Nanoparticle-Functionalized Tin Dioxide Nanowires via Radiolysis and Their Sensing Capability. *J. Mater. Res.* **2012**, *27*, 1688−1694.
(56) Byun, J.-H.; Katoch, A.; Choi, S.-W.; Kim, J.-H.; Kim, S. S. A Novel Synthesis Route for Pt-Loaded SnO_2 Nanofibers and Their Sensing Properties. *J. Nanosci. Nanotechnol.* **2014**, *14*, 8253−5257.
(57) Orozco, J. M.; Webb, G. The Adsorption and Hydrogenation of Benzene and Toluene on Alumina- and Silica- Supported Palladium and Platinum Catalysts. *Appl. Catal.* **1983**, *6*, 67−84.
(58) Minot, C.; Gallezot, P. Competitive Hydrogenation of Benzene and Toluene: Theoretical Study of Their Adsorption on Ruthenium, Rhodium, and Palladium. *J. Catal.* **1990**, *123*, 341−348.
(59) Paska, Y.; Haick, H. Interactive Effect of Hysteresis and Surface Chemistry on Gated Silicon Nanowire Gas Sensors. *ACS Appl. Mater. Interfaces* **2012**, *4*, 2604−2617.
(60) Traversa, E. Ceramic Sensors for Humidity Detection: The State-of-the-Art and Future Developments. *Sens. Actuators, B* **1995**, *23*, 135−156.
(61) Gong, J.; Chen, Q.; Lian, M.-R.; Liu, N.-C.; Stevenson, R. G.; Adami, F. Micromachined Nanocrystalline Silver Doped SnO_2 H_2S Sensor. *Sens. Actuators, B* **2006**, *114*, 32−39.
(62) Wang, C.; Yin, L.; Zhang, L.; Xiang, D.; Gao, R. Metal Oxide Gas Sensors: Sensitivity and Influencing Factors. *Sensors* **2010**, *10*, 2088−2106.

DOI: 10.1021/acsami.5b04066
ACS Appl. Mater. Interfaces 2015, 7, 17199−17208